Catalysis Science & Technology

ROYAL SOCIETY OF CHEMISTRY

PAPER

View Article Online
View Journal | View Issue

Cite this: *Catal. Sci. Technol.*, 2022, 12, 3582

Reaction pathways on N-substituted carbon catalysts during the electrochemical reduction of nitrate to ammonia†

Zheng Chen,‡[a] Jianhong Chen,‡[b] Giovanni Barcaro,[c] Tetyana M. Budnyak,[b] Anna Rokicińska, [d] Richard Dronskowski, [ae] Serhiy Budnyk,[f] Piotr Kuśtrowski, [d] Susanna Monti *[c] and Adam Slabon *[g]

Electrochemical reduction of nitrate into ammonia is one potential strategy to valorize pollutants needed to close the nitrogen cycle. The understanding of carbonaceous materials as metal-free representatives of electrocatalysts is of high importance to ensure sufficient activity and target selectivity. We report on the role of defects in cellulose-derived nitrogen-doped carbon (NDC) materials, produced by ammonolysis at different temperatures, to obtain efficient electrocatalysts for the nitrate reduction reaction (NO_3RR). Carbon catalyst ammonolysis at 800 °C (NDC-800) yields the highest electrochemical performance, exhibiting 73.1% NH_4^+ selectivity and nearly 100% NO_3^- reduction efficiency with a prolonged NO_3RR time (48 h) at −1.5 V *vs.* Ag/AgCl in a 0.1 M Na_2SO_4 electrolyte. We provide support to our findings by undertaking complementary structural analyses with scanning electron microscopy (SEM), transmission electron microscopy (TEM), powder X-ray diffraction (PXRD), X-ray photoelectron spectroscopy (XPS), Raman spectroscopy, low-temperature N_2 adsorption, and theoretical studies based on multi-scale/level calculations. Atomistic molecular dynamics simulations based on a reactive force field combined with quantum chemistry (QC) calculations on representative model systems suggest possible realistic scenarios of the material structure and reaction mechanisms of the NO_3^- reduction routes.

Received 10th January 2022,
Accepted 9th April 2022

DOI: 10.1039/d2cy00050d

rsc.li/catalysis

Introduction

Low-cost, high-performance carbon-based materials are metal-free catalysts that have the potential to challenge, as sustainable substitutes, established metal-based nanoparticle catalysts.[1–11] The most significant carbon-based materials are made from natural resources, and very often, cellulose is the preferential choice being the most abundant, renewable biopolymer on earth.[12–20] The cellulose macromolecule exists as a structural component of the primary cell wall in green plants, algae, and oomycetes, and is easily obtained from low-cost natural sources.[21] Notably, owing to its unique structure, it can be transformed by an environmentally friendly decomposition process at high temperatures, with low or even almost zero carbon emission, into cellulose-derived carbon substances.[12,16]

These products are then treated further to improve/maximize their performance in specific applications. Since the incorporation of heteroatoms could alter the properties of metal-free carbon materials, chemical doping with nitrogen was used to tailor their physicochemical properties effectively.[22–27] It was reported, in fact, that the incorporation of nitrogen improved their surface wettability, electron donor properties, conductivity, and reactivity.[3,28,29] Notwithstanding the successful results, a judicious choice of tailored functional modification is mandatory and crucial for manufacturing porous NDC materials as functional novel carbon materials.[3,30] As a matter of fact, the carbonization temperature and environmental conditions play essential roles in the tailored functional transformation, and their variation can drive the formation of porous structures and modulate the distribution of the incorporated nitrogen.[16,27]

The electrochemical NO_3RR, being characterized by much faster kinetics than the nitrogen reduction reaction (NRR), provides an attractive strategy to produce ammonia under ambient conditions and is considered a promising alternative to the Haber–Bosch process. Generally, the NO_3RR to ammonia

[a] *Institute of Inorganic Chemistry, RWTH Aachen University, 52056 Aachen, Germany*
[b] *Department of Materials and Environmental Chemistry, Stockholm University, 10691 Stockholm, Sweden*
[c] *CNR-ICCOM–Institute of Chemistry of Organometallic Compounds, 56124 Pisa, Italy*
[d] *Faculty of Chemistry, Jagiellonian University, ul. Golebia 24, 30-387 Krakow, Poland*
[e] *Hoffmann Institute of Advanced Materials, Shenzhen Polytechnic, 7098 Liuxian Blvd, Shenzhen, China*
[f] *AC²T research GmbH, Viktor-Kaplan-Str. 2c, 2700 Wiener Neustadt, Austria*
[g] *Inorganic Chemistry, University of Wuppertal, Gaußstr. 20, 42119 Wuppertal, Germany. E-mail: slabon@uni-wuppertal.de*

† Electronic supplementary information (ESI) available. See DOI: https://doi.org/10.1039/d2cy00050d

‡ These authors contributed equally to this work.

is more favorable than the NRR to ammonia due to the lower dissociation energy of the N=O bond (204 kJ mol^{-1}) than that of the N≡N bond (941 kJ mol^{-1}), as well as the higher solubility of nitrate in aqueous solution as compared to nitrogen gas.[31–43] The replacement of ion exchange, reverse osmosis, or bacterial denitrification with the electrochemical NO_3RR to ammonia is one of the most promising strategies to tackle nitrate degradation.[40–55] This methodology is based on the transformation of nitrate into ammonia that can be more easily recovered from its aqueous solution through regeneration of resins and converted into fertilizer.[44,52] The nitrate can also be turned into recyclable and valuable ammonia through renewable electricity inputs such as solar or wind sources. Nonetheless, the present electrocatalytic performance of the NO_3RR still suffers from a low ammonia yield rate at low at nitrate concentrations (<100 mg L^{-1}) due to the mass transfer.[31,32,35,39] On the other hand, the electrochemical NO_3RR involves complicated nine-proton and eight-electron transfer processes.[32] Numerous intermediates, such as toxic nitrous oxide, hydroxylamine, and diamine, may leak as by-products.[32] Consequently, the development of efficient catalysts should overcome current limitations, *e.g.* as low selectivity, low Faradaic efficiency, and release of toxic by-products.

To date, various metal-based catalysts have been reported for the electrochemical NO_3RR to ammonia.[31,56,57] The metal-free cellulose-derived NDC material as a perspective green electrocatalyst has received particular attention for electrocatalytic applications due to its significant electrical conductivity and catalytic activity that can be applied in the NO_3RR.[12,15,58] We have recently shown that graphitic N is important for NDC-800 in the electrochemical reduction of nitrite anions,[59] but the role of defects and the potential mechanisms in reduction of nitrate anions on carbon catalysts still remain elusive.

In this work, we disclose the reaction mechanisms for the electrochemical NO_3RR to ammonia on various NDC catalysts. The final optimized NDC electrocatalyst, under given conditions, exhibits high selectivity toward the ammonia synthesis from NO_3^- electroreduction with outstanding NO_3^- reduction efficiency.

Resorting to an efficient computational strategy based on reactive force field (ReaxFF) MD simulations at the atomic level as developed earlier[60] to create amorphous carbonaceous materials with different degrees of graphitization, we push the methodology steps forward, above the state of the art, by reproducing not only the whole carbonization of realistic cellulose fiber assemblies but also the N-doping process of the material. We have obtained representative models nicely matching the experimental results in terms of material density, graphitic character, and percentage of N and O atomic species. Then, we have identified the most critical NO_3^- binding sites by simulating the dynamics of the ion adsorption, which turn out to occur mainly in the defective regions. Then, as done before,[56,61,62] we have focused on small portions of the system. Indeed, we extracted a few representative locations and investigated them further through QC calculations to evaluate the energies involved in all the NO_3^- reduction reaction steps. Our findings match the literature extremely well, suggesting that nitrogen atoms in the defective regions could improve the reaction conditions.

Experimental section

Materials

Cellulose (microcrystalline, Sigma Aldrich) was used to prepare the NDC by the following steps. 3 g of cellulose was dried in a tube furnace under a 40 mL min^{-1} flow of N_2 at 250 °C for 6 h and then oxidized by soaking it in a 30 mL of 40 wt% HNO_3 aqueous solution at 50 °C for 3 h. Next, the resulting sample was centrifuged and washed with deionized water several times and subsequently dried overnight at 120 °C. The obtained materials were carbonized under a 20 mL min^{-1} flow of NH_3 and H_2 mixture at a constant temperature within the range of 500–900 °C for 2 h, with heating and cooling rates of 10 °C min^{-1}. The flow ratio of NH_3 and H_2 was selected to be 3 : 1 based on previous experience,[63,64] whilst the addition of H_2 was conducive to the equilibrium of the reversible reaction between NH_3 and H_2 with N_2 toward NH_3 at high temperatures. The resulting modified carbons were marked as NDC-500, NDC-600, NDC-700, NDC-800 and NDC-900 according to the carbonization temperatures of 500, 600, 700, 800, and 900 °C, respectively.

Structural characterization

N_2 adsorption. Analyses were conducted at −196 °C using an ASAP 2020 instrument (Micrometrics). The samples were degassed at 250 °C for 4 h under a dynamic vacuum before the measurement. The recorded data were analyzed using the following models: Brunauer–Emmett–Teller surface area (S_{BET}), Langmuir surface area ($S_{Langmuir}$), *t*-plot micropore volume (V_{micro}), and Barrett–Joyner–Halenda mesopore volume (V_{meso}). Moreover, the total pore volume (V_{total}) was determined by the single-point method ($p/p_0 \sim 0.99$).

PXRD. The diffraction patterns of the samples were recorded in transmission mode on a STOE STADI-P diffractometer using a Cu $K_{\alpha 1}$ radiation source, with a DECTRIS Mythen 1K detector. The measured 2θ range was detected from 10° to 60° with a scanning rate of 1° min^{-1}.

Raman spectroscopy. Spectra were recorded on a LabRAM HR 800 Raman instrument under excitation of 532 nm laser light with a power of 50 mW, where the laser was an air-cooled and double frequency Nd:YAG laser, and the intensity was adjusted using a filter wheel equipped with software-controlled 6ND filters.

Electron microscopy. SEM was performed on a Leo Supra 35VP SMT (Zeiss) thermal field emission scanning electron microscope and a JEOL JSM-7000F microscope. Copper tape was used for sample preparation for the SEM analysis. TEM was conducted on a JEOL-2100F.

Elemental analysis. Inductively coupled plasma optical emission spectrometry (ICP-OES) and a Flash 2000 elemental analyzer containing a thermal conductivity detector with an auto-sampler were used to determine the metal content and the C, H and N contents in the carbon materials, respectively.

XPS. Measurements were performed using a hemispherical analyzer (VG SCIENTA R3000) and monochromatized aluminum Al K_α radiation as an excitation source (E = 1486.6 eV). All the peaks were calibrated with an Au 4f reference peak at a binding energy of 84.0 eV. The recorded data were analyzed using the CasaXPS software.

Electrochemical measurements

For the preparation of the electrodes, typically, a carbon fiber (Toray carbon-paper TP-030, Quintech) was used as a substrate after ultrasonic cleaning with deionized water and ethanol for 15 min and drying under ambient atmosphere. The electrocatalyst ink was prepared by adding 6 mg of sample, 270 μL of ethanol, and 30 μL of Nafion (D-520 dispersion 5 wt%, Alfa Aesar) into a glass bottle, followed by treatment with ultrasound for 50 min. Subsequently, 100 mL of electrocatalyst ink was loaded onto each side of the carbon fiber in a multiple drop manner. The electrode was obtained after drying under ambient atmosphere for 2 h.

The electrochemical measurements were carried out using a potentiostat (Gamry Instruments) operating in a three-electrode setup. The prepared electrode, a platinum wire, and a 1 M Ag/AgCl electrode were used as the working electrode, counter electrode, and reference electrode, respectively. A relative-sealed typical H-type electrolytic cell separated by a Nafion 117 membrane was used as a reaction device. All the applied potentials were recorded against 1 M Ag/AgCl owing to the continuous change of the pH value during the electrochemical process. Milli-Q water (18.3 Ω cm) was used for the preparation of the electrolytes. Cyclic voltammetry (CV) and linear sweep voltammetry (LSV) were performed at a scan rate of 10 mV s^{-1}, and chronoamperometry (CA) was recorded at a stirring rate of 400 rpm for the NO_3RR. Before collecting data of the NO_3RR, the working electrode yielded a stable polarization curve and was cleaned with electrolyte while the fresh electrolyte of the electrolytic cell was bubbled with N_2 for 1 h.

Quantitative analysis

The concentrations of NO_3^-, NO_2^- and NH_4^+ were determined by spectrophotometry using an ultraviolet-visible (UV-vis) spectrophotometer (Genesys 10S) after diluting the samples to an appropriate concentration to match the range of the calibration curve. The following are the detailed methods and processes.

Determination of the nitrate concentration. An amount of electrolyte was taken out from the cathodic chamber and diluted to 5 mL. 0.1 mL of HCl (1 mol L^{-1}) and 0.01 mL of sulfamic acid solution (0.8 wt%) were successively added into the diluted electrolyte solution under shaking before being left to stand for 15 min. The calibration curve was achieved using different concentrations of $NaNO_3$ standard solutions and their corresponding absorbances (Fig. S1†). The absorbance was calculated according to the following formula:[44]

$$A = A_{220\text{nm}} - 2A_{275\text{nm}}$$

where A is the absorbance of nitrate, and $A_{220\text{nm}}$ and $A_{275\text{nm}}$ are the absorbances of nitrate at wavelengths of 220 nm and 275 nm, respectively.

Determination of the nitrite concentration. An amount of electrolyte was taken out from the cathodic chamber and diluted to 5 mL. One level microspoon reagent (114 658, MColortestTM) was added into the diluted electrolyte solution under shaking before being left to stand for 5 min. The absorbance was measured at a wavelength of 520 nm at 25 °C. The calibration curve was achieved using different concentrations of $NaNO_2$ standard solutions and their corresponding absorbances (Fig. S2†).

Determination of the ammonia concentration. 5 mL of electrolyte was taken out from the cathodic chamber to determine the ammonia concentration using 114 423 test kits (Merck Spectroquant). 0.4 mL of NH_4-1 reagent and 1 level microspoon NH_4-2 reagent were successively added into the solution under shaking before being left to stand for 5 min. Subsequently, 4 drops of NH_4-3 reagent were added before shaking for 10 s and being left to stand for 7 min. After that, the absorbance was measured at a wavelength of 655 nm at 25 °C. The calibration curve could be achieved using different concentrations of NH_4Cl standard solutions and their corresponding absorbances (Fig. S3†).

^{15}N isotope labelling experiments. The isotope labelling nitrate reduction experiments were carried out to clarify the source of ammonia. The above-mentioned electrochemical nitrate reduction methodology was used, except for the replacement of the N source with $Na^{15}NO_3$ (≥99%, Sigma Aldrich) at a concentration of 100 ppm of $^{15}NO_3^-$. The pH value of the electrolyte after the reaction was adjusted to weakly acidic with diluted H_2SO_4, and D_2O was added as an internal standard for further quantification by means of ^1H nuclear magnetic resonance (NMR) (400 MHz).

Calculation of the nitrate conversion, selectivity, Faradaic efficiency, and NH_4^+ yield. The NO_3^- conversion efficiency, NH_4^+ selectivity, NH_4^+ Faradaic efficiency, and NH_4^+ yield were calculated according to the following equations:

$$NO_3^- \text{ reduction efficiency} = \Delta C_{NO_3^-}/C_0 \times 100\%$$

$$NH_4^+ \text{ selectivity} = (C_{NH_4^+}/18) \times (\Delta C_{NO_3^-}/62) \times 100\%$$

$$NH_4^+ \text{ Faradaic efficiency} = (8F \times C_{NH_4^+} \times V) \times 18Q \times 100\%$$

$$NH_4^+ \text{ yield} = (C_{NH_4^+} \times V) \times (18 \times t \times m) \times 100\%$$

where C_0 is the initial concentration of NO_3^- (100 ppm); $\Delta C_{NO_3^-}$ is the concentration difference of NO_3^- between the

initial and final electrolyte (ppm); $C_{NH_4^+}$ is the final concentration of NH_4^+ (ppm); V is the electrolyte volume (50 mL); F is the Faradaic constant (96 485 C mol^{-1}); Q is the total charge used for the carbon (C); t is the time of electrolysis (h); m is the mass of the catalyst (2 mg).

Multi-level/scale calculations

Molecular dynamics simulations. To disclose the chemical evolution and dynamics of the different materials during carbonization in terms of the degree of graphitization, general morphology, the content of hydrogen, nitrogen, and oxygen, their hybridization, and distribution, we designed a specific computational strategy, which could mimic the different stages of the process starting from the original preassembled components in agreement with the experiments. The molecular model used as a starting material consisted of cellulose fibers parallelly packed in a rectangular parallelepiped box.

Eight cellulose fibers, made of sixteen chains with sixteen glucosyl residues each, arranged as a parallelepiped rod (84 × 25 × 25 $Å^3$), were assembled parallelly close to each other on two parallel planes (four fibers on each plane – Fig. S4†) and used as the carbon source in the carbonization process. This was reproduced through all-atom reactive molecular dynamics (RMD) simulations based on a pre-parametrized force field using the MD-ReaxFF code implemented in the Amsterdam Density Functional (ADF)/ReaxFF package.[65,66] The size of the simulation box was fixed at 100 × 100 × 100 $Å^3$. Carbonization was simulated through RMD runs at high and low temperatures in the *NVT* ensemble, applying periodic boundary conditions in all directions (Fig. S5 and S6†). Then, nitrogen atoms were introduced in the simulation box, and the dynamics run was extended to thermalize and stabilize the new system at a high temperature and induce the internalization of the N atoms (Fig. S7–S9†).[60] This was useful for estimating the capacity of adsorption of the carbonized material and possible types of insertion. The final equilibrated model (Fig. S7†) was selected for the subsequent simulations in the presence of NO_3^- ions.

A stable carbonized N-doped configuration extracted from the final portion of the RMD trajectory was surrounded by NO_3^- ions, equilibrated in the *NVT* ensemble at ambient temperature and simulated for about 200 ps. The final configuration was used to identify probable locations of the ions close to the graphitic regions (Fig. S10 and S11†). No restraints were applied to the systems, and reactivity was always on to simulate bond breaking and formation in response to the surrounding environment. All the details of the simulations are reported in the ESI.†

QC calculations. After explorative QC optimizations of various model systems extracted from the simulations and modified to comply with the QC requirements (see ESI† – Fig. S12–S14), which were meant to provide qualitative descriptions of the chains of reactions taking place on the catalyst, we opted for a more systematic approach to provide quantitative estimates of the energies that came into play. Thus, selected portions of the RMD configurations were used to build the QC models aimed at reconstructing the whole mechanism of the NO_3RR under realistic conditions. All QC calculations were carried out with the Quantum Espresso package[67] in conjunction with the GGA-PBE xc-functional,[68] the Grimme-D2 corrections (to account for van der Waals dispersion interactions),[69] and ultrasoft pseudo-potentials. Local relaxations were performed spin-polarized, applying 40 Ry and 400 Ry cut-offs on the one-electron wave functions and density, respectively. The single-particle KS levels were broadened by Gaussian smearing of 0.002 Ry. The first Brillouin zone was sampled at the Γ point only, as the selected systems were intrinsically non-periodic; for this purpose, a minimum empty space of 10–15 Å in all directions was selected in order to decouple the system from its replicas. Our approach and the process analysis were inspired by previous investigations focused on similar processes.[56,61] Reaction energies were calculated referring to a gas-phase HNO_3 molecule and the hydrogen electrode method,[62] which assumes that the chemical potential of an electron–proton pair is equal to that of $1/2H_2$ in the gas phase. The limiting potential of each mechanism was calculated by taking the negative of the maximum energy difference between every two successive steps in the mechanism diagram. Reaction energies were calculated in the gas phase by considering the effects played by the insertion of solvation models negligible.

Results and discussion

Characterization

As a carbon-based material formed by the oxidation of cellulose by HNO_3 and then carbonization under an NH_3/H_2 flow, NDC has a porous structure with a large surface area. Irregular shapes and disordered open pores of the particles are visible in the SEM and TEM micrographs (Fig. 1) of the five NDC materials, *i.e.*, NDC-500, NDC-600, NDC-700, NDC-800 and NDC-900. Further analysis of these porous materials by means of N_2 adsorption (Fig. 2a) revealed that the shape of the isotherms strongly depends on the carbonization temperature. The N_2 uptake for NDC-500 and NDC-600 is very low, suggesting the non-porous character of these materials,

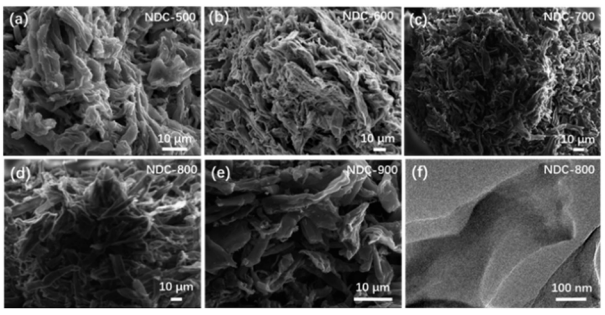

Fig. 1 SEM micrographs of (a) NDC-500, (b) NDC-600, (c) NDC-700, (d) NDC-800 and (e) NDC-900; (f) TEM image of NDC-800.

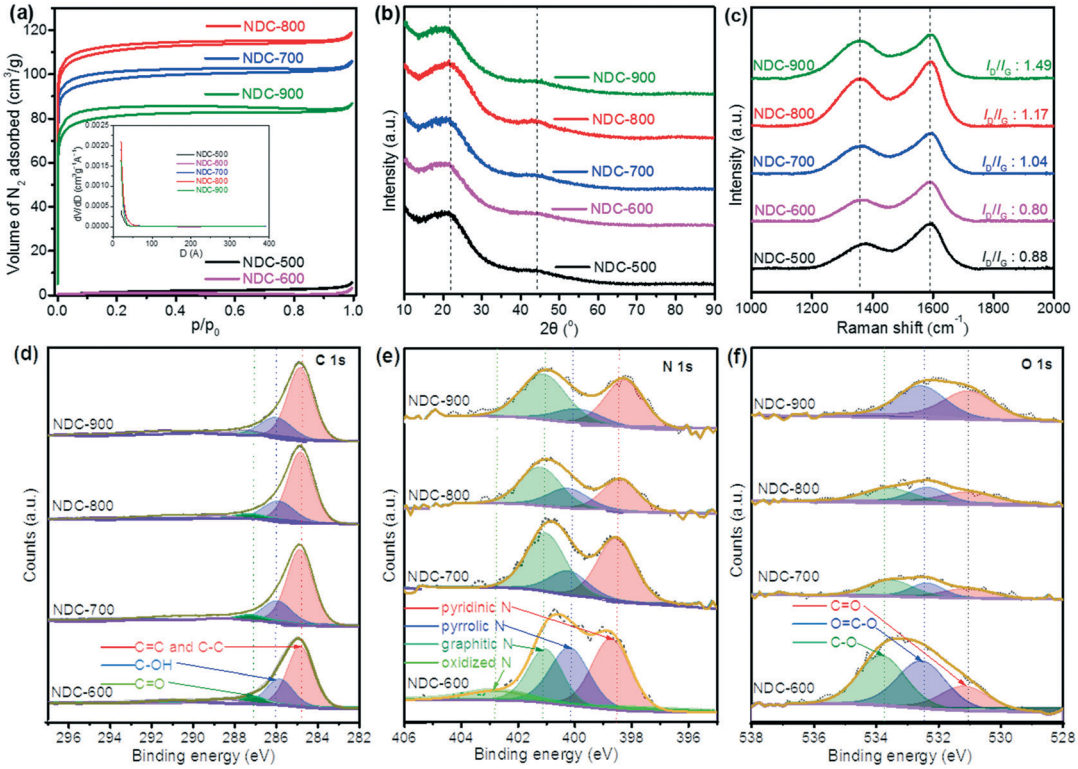

Fig. 2 (a) N_2 adsorption–desorption isotherms, (b) PXRD patterns and (c) Raman spectra of NDC-500, NDC-600, NDC-700, NDC-800 and NDC-900 materials; XPS (d) C 1s, (e) N 1s and (f) O 1s spectra of NDC-600, NDC-700, NDC-800 and NDC-900 materials.

whereas the samples carbonized at higher temperatures show adsorption isotherms of type I according to the IUPAC classification.[70] This type of isotherm assesses microporous materials where the limiting adsorbate uptake is governed by the accessible micropore volume rather than by the internal surface area. As shown in Table 1, NDC-800 had a higher total pore volume (V_{total} = 0.184 $cm^3\ g^{-1}$) and BET surface area (S_{BET} = 413 $m^2\ g^{-1}$) than the others. The surface area and porosity could decrease due to the material shrinkage at high temperatures (900 °C).[70]

These observations well compare with the final morphology of the atomistic model extracted from the carbonization doping RMD simulations. The typical structures (Fig. S7–S9†) consist of an extended network of graphene-like sheets with nonlinear bending deformations, several contortions, defects, and vacancies. These became more randomly twisted, rugged, and packed in the central region of the simulation box, where the material was accumulated and formed a sort of a long carbon fiber (visible through periodicity). The combination of these atomistic shapes might generate the macroscopic morphology shown in Fig. 1. Planar motifs (graphitized sheets) interconnecting the fibers were found at the boundaries (Fig. 3). We could estimate the degree of graphitization considering the bond orders of the atoms in the structure, and we found that the ratio between the graphitic-like and diamond-like carbon was about 1.44, confirming the dominant graphitic character of the ensemble. The composition of the final structured configurations is approximately C 88%, N 6%, and O 1%. Most of the O and N atoms are on the edges of the pores. O is bound as C═O and C–O–C, whereas N is more prone to ring insertion. 10% of the total number of nitrogen is inserted in carbon rings. 25% is found in five-membered-rings, 45% in six-membered-rings, 21% in seven-membered-rings and 8% in eight-membered-rings. These rings could be inside the core of the structure or at the edges of the pores. Only 6% of the nitrogen is inside the graphitic sheets, while the other nitrogen atoms are bonded to carbon chains at the boundaries of the fibers. The analysis of the pore size distribution, evaluated with the CAVER software, revealed the presence of pores in the range of 2–3 nm (Fig. S9†) inside the fiber, which is in good agreement with the experimental findings.

Table 1 Textural parameters from the five NDC materials after carbonization at different temperatures in a flow of NH_3/H_2

Sample	S_{BET} ($m^2\ g^{-1}$)	$S_{Langmuir}$ ($m^2\ g^{-1}$)	V_{total} ($cm^3\ g^{-1}$)	V_{meso} ($cm^3\ g^{-1}$)	V_{micro} ($cm^3\ g^{-1}$)
NDC-500	6	12	0.009	0.006	0.001
NDC-600	3	5	0.005	0.001	0.001
NDC-700	357	437	0.164	0.136	0.017
NDC-800	413	494	0.184	0.154	0.019
NDC-900	304	362	0.135	0.113	0.012

Indeed, the determination of the chemical composition of the five NDC materials *via* elemental analysis reveals that the materials consist mainly of C, N, and H (Table 2). It should be noted that these samples also contain significant amounts

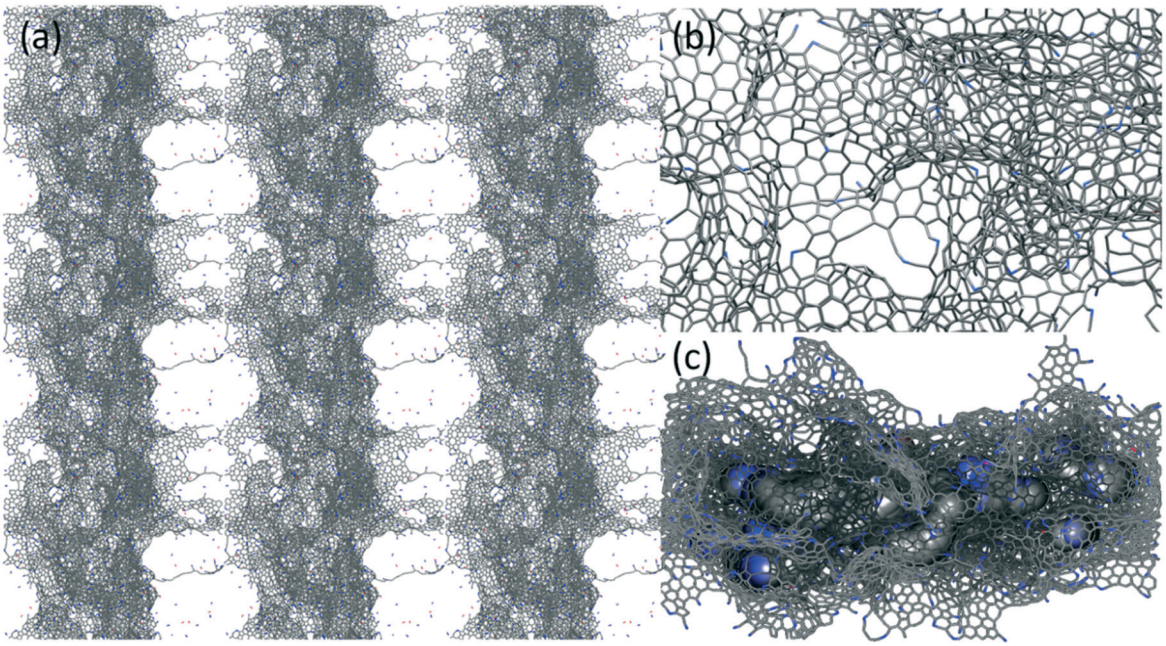

Fig. 3 (a) The final carbonized-N-doped atomistic configuration obtained through RMD (periodic replica), (b) graphitic-like structure with N at the edges of the pores, and (c) identification of the tunnels and cavities by CAVER's sphere filling (stick models and spheres colored according to the atom type: C gray, O red, N blue).

of oxygen, which cannot be determined by this method. A downward trend of the resultant N and H contents was observed with the increase in the carbonization temperature since pyrolysis at high temperature accelerates the break-up of the N-containing networks. The increase in N content at 900 °C can be explained by the reaction of the material with nitrogen due to the presence of ammonia during calcination at high temperatures.[16,22,27,30] In addition, further analysis with ICP revealed the low concentrations (<10 ppm) for Cr, Mn, Ni, Co, Cu, Mo, V, W, Pt, and Pd in the NDC materials.

The structural identification of the NDC materials through multiple analytical techniques showed that the PXRD patterns present two broad diffraction feature peaks at 23° and 44° assigned to the graphite facets (002) and (101) of carbon (Fig. 2b).[9] Raman spectral analysis reveals D and G bands at 1340 cm^{-1} and 1590 cm^{-1} (Fig. 2c), respectively. Both D and G bands arise from the disordered sp^2 hybridized carbon and the crystalline graphitic carbon, respectively.[71] The ratio intensity of the D and G bands (I_D/I_G) is considered an essential asset to evaluate the degree of graphitization of carbon materials. A trend of higher ratios was observed upon increasing the carbonization temperature, whilst NDC-900 had the highest I_D/I_G ratio (1.49), implying more defects and disordered structures than the others.[72] XPS disclosed the surface composition of the materials (Fig. 2d–f), which showed that the ratio of resultant pyrrolic N decreased while that of total graphitic and pyridinic N increased with the increase of carbonization temperature. Graphitic N and pyridinic N are considered efficient and stable metal-free active sites, which are closely related to the electrocatalysis properties of NDC materials.[3,28,29]

Table 2 C, H, and O and their relative contents in the five NDC materials

Sample	C%	N%	H%
NDC-500	71.9	8.0	3.6
NDC-600	76.5	9.0	2.6
NDC-700	82.4	7.7	1.8
NDC-800	84.0	5.7	1.4
NDC-900	82.1	6.3	1.4

Catalysis

Since the carbonization temperature can affect the formation of the carbon-based catalyst structure and thus its electrocatalytic activities, we tested various carbonization temperatures to select the best conditions and prepared a series of cellulose-derived NDC samples, namely NDC-500, NDC-600, NDC-700, NDC-800, and NDC-900.

Then, we measured the electrochemical NO_3RR in a 0.1 M Na_2SO_4 electrolyte with 100 ppm NO_3^- (pH 5.6). The results are depicted in Fig. 4a. Among the five NDC materials, the highest electrocatalytic activity was achieved for the NDC-800 catalyst. This trend was also typical for the hydrogen evolution reaction (HER) at lower potentials (Fig. S15†) and the oxygen evolution reaction (OER) at higher potentials (Fig. S16†) in a 0.1 M NaOH electrolyte. Furthermore, NDC-800 yielded 28.1 ppm NO_2^- and 2.09 ppm NH_4^+ from the NO_3RR in CA at −1.5 V *vs.* Ag/AgCl for 2 h, with the highest NH_4^+ Faradaic and NO_3^- reduction efficiencies (Fig. 4b). Although the five NDC materials had similar textural properties, the presented electrocatalytic activity of the electrochemical

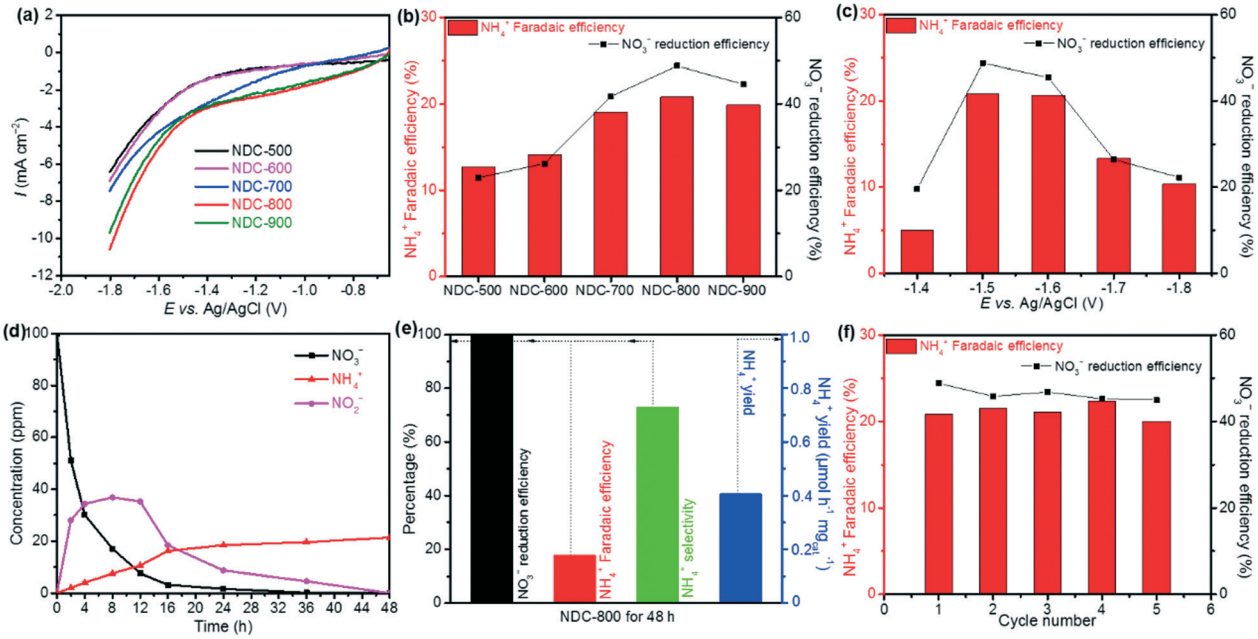

Fig. 4 (a) LSV curves of NDC-500, NDC-600, NDC-700, NDC-800 and NDC-900 for the NO_3RR; (b) NH_4^+ Faradaic and NO_3^- reduction efficiencies of NDC-500, NDC-600, NDC-700, NDC-800 and NDC-900 at −1.5 V *vs.* Ag/AgCl for 2 h CA; (c) NH_4^+ Faradaic and NO_3^- reduction efficiencies of NDC-800 at various applied potentials for 2 h CA; (d) time-dependent concentrations of NO_3^-, NO_2^- and NH_4^+ over NDC-800 CA at −1.5 V *vs.* Ag/AgCl; (e) NO_3^- reduction efficiency, NH_4^+ Faradaic efficiency, NH_4^+ selectivity and NH_4^+ yield of NDC-800 at −1.5 V *vs.* Ag/AgCl for 48 h CA; (f) NO_3^- reduction and NH_4^+ Faradaic efficiencies of NDC-800 at −1.5 V *vs.* Ag/AgCl for 2 h CA after consecutive recycling tests. Measurements were performed in a 0.1 M Na_2SO_4 aqueous electrolyte with 100 ppm of NO_3^-.

NO_3RR climbs up first and then declines when the carbonization temperature increases from 500 °C to 900 °C (Fig. 4b). From these findings, we could speculate that the significant activity of NDC-800 in the electrochemical NO_3RR is related to its higher microporosity and a more substantial number of active sites rather than a higher amount of nitrogen. This is demonstrated by the computational multi-scale approach that not only identified the active sites as the defective regions where undercoordinated/open valence atoms were present but also reproduced the dynamics of the NO_3^- ions towards these locations and the whole reaction mechanisms. In summary, the experiments indicate that ammonolysis at 800 °C can create an optimum NDC structure for the efficient electrochemical NO_3RR to ammonia.

Thus, we chose NDC-800 to identify the optimum applied potential for the catalytic activity for the NO_3RR. The measurements were performed in a 0.1 M Na_2SO_4 electrolyte with 100 ppm NO_3^- on CA for 2 h, at constant potentials of −1.4, −1.5, −1.6, −1.7, and −1.8 V *vs.* Ag/AgCl. As shown in Fig. 4c, the yield of NH_4^+ and the current density increased upon increasing the applied potentials. Due to the competition with competitive reactions, such as the HER and nitrite reduction reaction (NO_2RR), both NO_3^- reduction and NH_4^+ Faradaic efficiencies showed a volcanic shape curve with a maximum value of 48.8% and 20.8% at −1.5 V *vs.* Ag/AgCl, respectively.

Unveiling the electrocatalytic decay rate of the NO_3^- concentration with reaction time could provide crucial information on removed NO_3^- for the NDC-800 material toward the possibility of using it in NO_3RR application. Therefore, further studies in this system and CA measurements were performed at −1.5 V *vs.* Ag/AgCl in a 0.1 M Na_2SO_4 electrolyte with 100 ppm NO_3^- for 2, 4, 8, 12, 16, 24, 36, and 48 h. The results of time-dependent NO_3^-, NO_2^- and NH_4^+ concentrations are shown in Fig. 4d. As the reaction time increased, better effective reduction efficiency of NO_3^- was observed and reached nearly 100% when prolonging to 48 h, while the intermediate by-product NO_2^- concentration increased first and was further almost completely electrochemically reduced to NH_4^+ after 48 h. The concentration of NH_4^+ increased, with an NH_4^+ faradaic efficiency of 17.8%, selectivity of 73.1%, and NH_4^+ yield rate of 0.42 μmol h^{-1} $mg_{cat.}^{-1}$ (Fig. 4e). The metal-free NDC-800 exhibited high selectivity toward the ammonia synthesis from NO_3^- electroreduction with outstanding reduction efficiency.

The stability of the NDC-800 catalyst during the NO_3RR was estimated by means of consecutive recycling tests using the same electrode before cleaning and drying. Each cycle of tests was carried out for 2 h using CA at −1.5 V *vs.* Ag/AgCl in a 0.1 M Na_2SO_4 electrolyte with 100 ppm NO_3^-. The results of five cycling tests are depicted in Fig. 4f. Notably, the CA plots showed only a slight fluctuation and no apparent downward trend. Meanwhile, the remaining amount of NO_3^-, the yield of NO_2^- and NH_4^+, the NO_3^- reduction efficiency, and the NH_4^+ Faradaic efficiency revealed small changes but no evident trend of decrease after each test. These results imply good catalytic stability during the NO_3RR for the NDC-800

catalyst, which is consistent with previous carbon-based materials studies.[59,73]

To verify the source of ammonia, the electrolyte without NO_3^- was also tested as a control experiment for the electrochemical NO_3RR. The result showed that the electrochemical NO_3RR measured in blank Na_2SO_4 electrolyte yielded a negligible concentration of NH_4^+ (Fig. 5). Meanwhile, ^{15}N isotope labeling ^1H NMR spectra were acquired to further verify the source of ammonia. The ^1H NMR spectra of the electrolyte after the NO_3RR with $Na^{15}NO_3$ at −1.5 V *vs.* ref for 2 h show typical double peaks of $^{15}NH_4^+$, which is different from the triple peaks of $^{14}NH_4^+$ from the ^1H NMR spectra with $Na^{14}NO_3$ as the reactant (Fig. 6).[74] This result further confirms that the produced NH_4^+ originates from the electrochemical reduction of NO_3^-.

Reaction mechanisms by multi-scale/level calculations

To investigate the reaction mechanism and unravel the origin of NDC's high performance in the NO_3RR, we performed density functional theory (DFT) calculations starting from the RMD supramolecular model described above. Considering that nitrate reduction to ammonia can take place according to several mechanisms and that only defects (low-coordinated sites) resulted as active centers towards nitrate reduction,[56,75] we carefully scrutinized the process against a typical defect site of the NDC material identified in the RMD simulations.

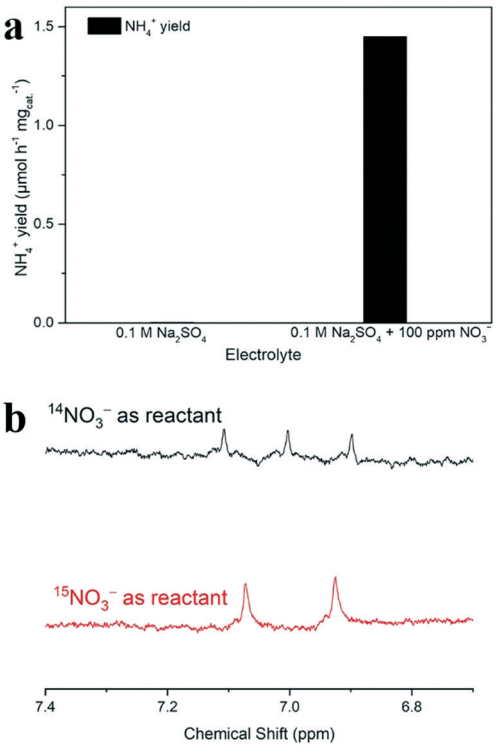

Fig. 5 (a) NH_4^+ yield of NDC-800 in 0.1 M Na_2SO_4 electrolyte with and without 100 ppm NO_3^- for 2 h CA; (b) ^1H NMR spectra of the electrolyte after the electrocatalytic NO_3RR using $^{15}NO_3^-$ and $^{14}NO_3^-$ as the nitrogen sources.

The analysis of the corresponding energy profiles (Fig. S17 and S18†) allowed the identification of a promising reduction pathway with limiting potentials in a range of the experimental onset potentials at −1.50 V *vs.* Ag/AgCl accompanied by eight proton/electron transfers and the generation of ammonia (and water molecules). The detailed steps of such a pathway are shown in Fig. 6. It is easy to notice that the initially two O atoms of HNO_3 (under acidic conditions, RMD simulations predicted the stabilization of the nitrate ion as undissociated nitric acid) strongly interact with the defect and spontaneously dissociate nitric acid into NO (not in direct contact with the surface), an oxygen atom and a hydroxyl group anchored to the defect borders (step 1 in Fig. 6). The addition of a proton/electron pair leads to the spontaneous generation (downhill energy variation) of a water molecule released into the environment (step 2). The oxygen atom firmly bound to the defect can generate a second water molecule *via* the addition of two further proton/electron pairs (steps 3 and 4) *via* an uphill variation characterized by a limiting potential of about −1.2 eV.

Interestingly, a modification of the defect borders, achieved by inserting a nitrogen atom, as shown in Fig. 7, can decrease (in absolute value) the limiting potential of such a step to about −0.6 eV. The reduction proceeds *via* the adsorption of NO in the surface defects. We simulate this scenario by considering the adsorption of NO on the most strongly interacting carbon atom of the defective region (the atom with only two first neighbors). It is worth mentioning that this is a very subtle step as the adsorption could be *via* the N or the O atom, and thus the reduction could proceed through different mechanisms. More specifically, the adsorption *via* the N atoms evolves by those mechanisms labeled in the literature as O-distal, O-alternating, N-distal, and N-alternating. Such mechanisms, whose energy plots are reported in the ESI,† are characterized by downhill steps up to the stabilization of the NH_2 species strongly interacting with the defect borders and characterized by limiting potentials (larger than −1.8 eV in absolute values) that are too high for the generation of ammonia.

Instead, if the adsorption of NO takes place according to the configuration depicted in step 5 of Fig. 6 (where it is the O atom that is connected to the carbon with the most robust interaction), the reduction can proceed according to other mechanisms labeled N-first, N-enzymatic, O-first, and O-enzymatic, which are more convenient. Among these, it is the N-first that results as the most promising mechanism, and it corresponds to the mechanism depicted in Fig. 6. Starting from configuration 5, NO can adsorb two H atoms *via* the addition of two proton/electron pairs, resulting in the adsorbed HNO and H_2NO species (steps 6 and 7); the first step is downhill in energy, whereas the second one is characterized by a relatively low (about −0.4 eV) limiting potential. Further proton/electron addition produces ammonia (step 8) and leaves on the surface an adsorbed O atom in an analogous configuration to that of step 2. In fact, the generation of the last water molecule (steps 9 and 10) proceeds *via* the addition of the final two proton/

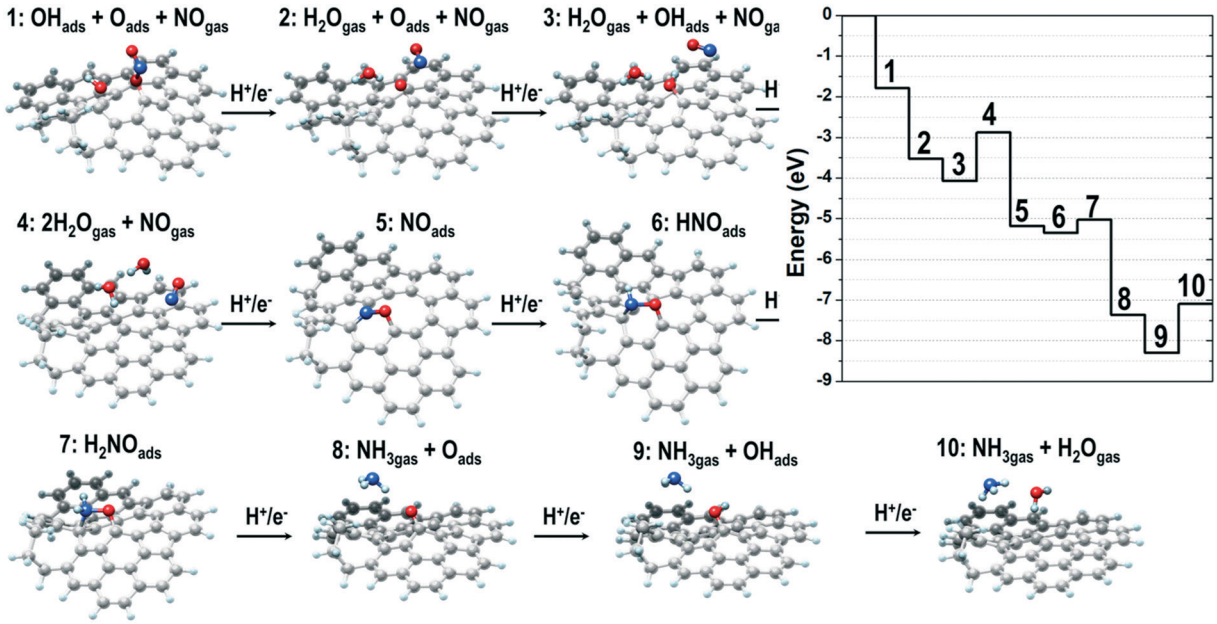

Fig. 6 Energy profile of the NO_3RR mechanism leading to the formation of NH_3 and three water molecules and the corresponding configurations. These were obtained through energy minimizations at the QC level (using a reduced model system terminated with hydrogen atoms). C gray, N blue, O red, H light blue. Note that the first step is the spontaneous dissociation of HNO_3 at the carbon surface.

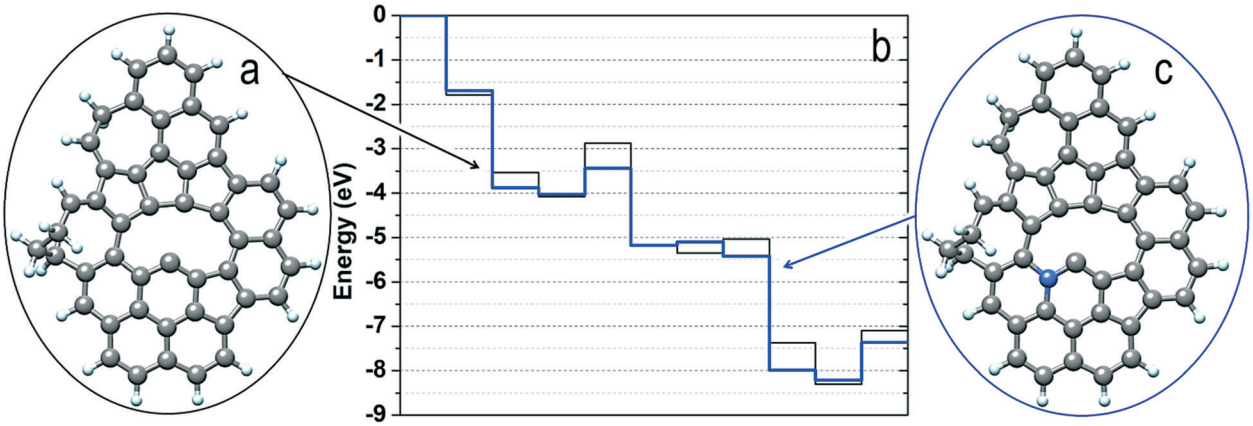

Fig. 7 (a) Structure of the bare defect sampled as the catalytic site in the mechanism shown in Fig. 6; (b) energy profiles for the NO_3RR mechanism characterizing sites (a) and (c); (c) same structure of panel (a) where one C atom next to the defect border has been replaced with a nitrogen atom.

electron pairs with a profile very similar to that observed in steps 3 and 4 and a limiting potential of about −1.2 eV. If we consider the defect in the presence of the N atom at the border of the defect, Fig. 7, this last limiting potential is decreased (in absolute value) to about −0.8 eV, analogous to what was observed for the generation of the second water molecule.

We want to point out that here we do not present the precise topology of the defect as the only candidate for promoting nitrate reduction, and the models we used are aimed at demonstrating the presence of a family of localized surface defects (whose formation derives from the chosen synthetic procedure) with catalytic properties associated to limiting potentials in agreement with the experimentally observed onset potentials. A further degree of freedom is given by the composition of the final cellulose-derived NDC material, as it has been explicitly shown that the presence of N atoms can modulate the catalytic properties of the neighboring sites. Furthermore, the described N-first mechanism is characterized by limiting potentials in the range of −0.6/−1.2 eV, corresponding to water evolution and the polishing of the surface borders from adsorbed O atoms or OH groups. The production of NH_3 is achieved at much lower (in absolute values) limiting potentials, corresponding, in the aforementioned case, to about −0.4 eV. This means that working at −1.5 V *vs.* Ag/AgCl does not guarantee (according to our analysis) the removal of oxygen species from the defect borders but guarantees the evolution of ammonia *via* an N-first mechanism.

We could speculate that the active site, besides binding oxygen and nitrogen, can also modulate the interaction of intermediates, thus optimizing the reaction pathway and hindering the formation of by-products. This is consistent with the experimental results that identified NDC-800, which displayed more active sites, as the more active catalyst.

Conclusions

In summary, metal-free cellulose-derived NDC materials were synthesized as electrocatalysts. NDC-500, NDC-600, NDC-700, NDC-800, and NDC-900 were prepared from cellulose with a combination of HNO_3 treatment and carbonization with NH_3/H_2 at 500, 600, 700, 800, and 900 °C, respectively. For the electrochemical NO_3RR performed at the optimal potential of −1.5 V *vs.* Ag/AgCl in a 0.1 M Na_2SO_4 electrolyte with 100 ppm NO_3^-, the NDC-800 material exhibited higher electrocatalytic activity in comparison with the other materials, showing 73.1% NH_4^+ selectivity toward the ammonia synthesis from NO_3^- electroreduction and nearly 100% NO_3^- reduction efficiency when prolonging to 48 h, with outstanding electrochemical stability. We have provided a complete computational description of the NDC material, from the formation to the catalytic activity. This has not been carried out yet for these types of amorphous systems due to their complex nature and organization. Using ReaxFF MD simulations, we have simulated all the processes leading to the carbonized-N-doped morphologies starting from the cellulose fibers and obtained realistic models of the NDC catalyst corresponding to the experimental findings (as confirmed by analysis of the structures). We have described, at the atomic level and on the nanoscale region, the behavior of the system in terms of morphology, distinct reactive regions, and ion adsorption. We have identified the most active portions and explored through QC calculations (at the sub-nanoscale) the reaction mechanisms there to disclose the role played by the N-doping action and the energies involved in the formation of the final products. The results suggest that defective regions containing nitrogen atoms are fundamental to improving the material response and agree with the general picture that emerged from the experimental characterization. This synergistic combination of all the experimental techniques and computational modeling can be used effectively for careful design of efficient carbon-based catalysts for the electrochemical NO_3^- reduction to ammonia.

Data availability

The datasets supporting this article have been uploaded as part of the ESI.†

Author contributions

Z. C. synthesized the materials and performed the Raman analysis. J. C. performed the electrochemical and TEM experiments. S. M and G. B. performed the theoretical calculations and analyzed the work. A. R. and P. K. performed the N_2 adsorption, CHN analysis and XPS measurements. R. D. co-supervised the synthesis and analysis. A. S. and S. M. supervised the project and designed the experiments and calculations. All authors contributed to the writing of the manuscript. All authors have given approval to the final version of the manuscript.

Conflicts of interest

There are no conflicts to declare.

Acknowledgements

This work was financially supported by the Swedish Energy Agency (project nr: 50501-1). Z. C. would like to thank the China Scholarship Council for a PhD scholarship. P. K. acknowledges the European Regional Development Fund in the framework of the Polish Innovation Operational Program (contract no. POIG.02.01.00-12-023/08) for financial support. T. M. B. acknowledges the Swedish Research Council for Sustainable Development Formas (project reg. nr: 2020-02321) for financial support. S. B. thanks the "Austrian COMET-Program" (project InTribology1, no. 872176) *via* the Austrian Research Promotion Agency (FFG) and the federal states of Niederösterreich and Vorarlberg, which was carried out within the "Excellence Centre of Tribology" (AC2T research GmbH).

Notes and references

1 D. Liu, L. Dai, X. Lin, J. F. Chen, J. Zhang, X. Feng, K. Müllen, X. Zhu and S. Dai, *Adv. Mater.*, 2019, **31**, 1804863.
2 Y. Song, W. Chen, C. Zhao, S. Li, W. Wei and Y. Sun, *Angew. Chem., Int. Ed.*, 2017, **56**, 10840–10844.
3 Y. Yang, L. Gu, S. Guo, S. Shao, Z. Li, Y. Sun and S. Hao, *Front. Chem.*, 2019, **7**, 1–18.
4 Y. Zhao, R. Nakamura, K. Kamiya, S. Nakanishi and K. Hashimoto, *Nat. Commun.*, 2013, **4**, 1–7.
5 Q. Lv, W. Si, J. He, L. Sun, C. Zhang, N. Wang, Z. Yang, X. Li, X. Wang, W. Deng, Y. Long, C. Huang and Y. Li, *Nat. Commun.*, 2018, **9**, 1–11.
6 C. Zhang, N. Mahmood, H. Yin, F. Liu and Y. Hou, *Adv. Mater.*, 2013, **25**, 4932–4937.
7 K. Tian, J. Wang, L. Cao, W. Yang, W. Guo, S. Liu, W. Li, F. Wang, X. Li, Z. Xu, Z. Wang, H. Wang and Y. Hou, *Nat. Commun.*, 2020, **11**, 2–11.
8 X. Wang, A. Vasileff, Y. Jiao, Y. Zheng and S. Z. Qiao, *Adv. Mater.*, 2019, **31**, 1803625.
9 H. Jiang, J. Gu, X. Zheng, M. Liu, X. Qiu, L. Wang, W. Li, Z. Chen, X. Ji and J. Li, *Energy Environ. Sci.*, 2019, **12**, 322–333.
10 R. Pawlak, X. Liu, S. Ninova, P. D'Astolfo, C. Drechsel, S. Sangtarash, R. Häner, S. Decurtins, H. Sadeghi, C. J. Lambert, U. Aschauer, S. X. Liu and E. Meyer, *J. Am. Chem. Soc.*, 2020, **142**, 12568–12573.
11 T. Zhang, W. Schilling, S. U. Khan, H. Y. V. Ching, C. Lu, J. Chen, A. Jaworski, G. Barcaro, S. Monti, K. De Wael and A. Slabon, *ACS Catal.*, 2021, **11**, 14087–14101.

12 R. J. Moon, A. Martini, J. Nairn, J. Simonsen and J. Youngblood, *Chem. Soc. Rev.*, 2011, **40**, 3941–3994.
13 X. Wu, Z. Shi, R. Tjandra, A. J. Cousins, S. Sy, A. Yu, R. M. Berry and K. C. Tam, *J. Mater. Chem. A*, 2015, **3**, 23768–23777.
14 P. Song, B. Liu, C. Liang, K. Ruan, H. Qiu, Z. Ma, Y. Guo and J. Gu, *Nano-Micro Lett.*, 2021, **13**, 1–17.
15 X. Du, Z. Zhang, W. Liu and Y. Deng, *Nano Energy*, 2017, **35**, 299–320.
16 H. Wang, Y. Shao, S. Mei, Y. Lu, M. Zhang, J. K. Sun, K. Matyjaszewski, M. Antonietti and J. Yuan, *Chem. Rev.*, 2020, **120**, 9363–9419.
17 T. Bai, Y. Guo, D. Wang, H. Liu, G. Song, Y. Wang, Z. Guo, C. Liu and C. Shen, *J. Mater. Chem. A*, 2021, **9**, 5566–5577.
18 B. P. Chhetri, D. Soni, A. B. Rangumagar, C. M. Parnell, H. Wayland, F. Watanabe, G. Kannarpady, A. S. Biris and A. Ghosh, *J. Environ. Chem. Eng.*, 2017, **5**, 2586–2596.
19 C. Chen, Y. Kuang, S. Zhu, I. Burgert, T. Keplinger, A. Gong, T. Li, L. Berglund, S. J. Eichhorn and L. Hu, *Nat. Rev. Mater.*, 2020, **5**, 642–666.
20 R. Huang, C. Cao, J. Liu, D. Sun and W. Song, *Chem. Commun.*, 2019, **55**, 1935–1938.
21 T. Li, C. Chen, A. H. Brozena, J. Y. Zhu, L. Xu, C. Driemeier, J. Dai, O. J. Rojas, A. Isogai, L. Wågberg and L. Hu, *Nature*, 2021, **590**, 47–56.
22 Z. Qiang, Y. Xia, X. Xia and B. D. Vogt, *Chem. Mater.*, 2017, **29**, 10178–10186.
23 D. Deng, X. Pan, L. Yu, Y. Cui, Y. Jiang, J. Qi, W. X. Li, Q. Fu, X. Ma, Q. Xue, G. Sun and X. Bao, *Chem. Mater.*, 2011, **23**, 1188–1193.
24 Y. Cao, S. Mao, M. Li, Y. Chen and Y. Wang, *ACS Catal.*, 2017, **7**, 8090–8112.
25 X. Y. Wang, X. Yao, A. Narita and K. Müllen, *Acc. Chem. Res.*, 2019, **52**, 2491–2505.
26 T. Schiros, D. Nordlund, L. Pálová, D. Prezzi, L. Zhao, K. S. Kim, U. Wurstbauer, C. Gutiérrez, D. Delongchamp, C. Jaye, D. Fischer, H. Ogasawara, L. G. M. Pettersson, D. R. Reichman, P. Kim, M. S. Hybertsen and A. N. Pasupathy, *Nano Lett.*, 2012, **12**, 4025–4031.
27 W. Luo, B. Wang, C. G. Heron, M. J. Allen, J. Morre, C. S. Maier, W. F. Stickle and X. Ji, *Nano Lett.*, 2014, **14**, 2225–2229.
28 Z. Zhang, L. Yu, Y. Tu, R. Chen, L. Wu, J. Zhu and D. Deng, *Cell Rep. Phys. Sci.*, 2020, **1**, 100145.
29 N. Zhou, N. Wang, Z. Wu and L. Li, *Catalysts*, 2018, **8**, 509.
30 Y. Liu, Y. Su, X. Quan, X. Fan, S. Chen, H. Yu, H. Zhao, Y. Zhang and J. Zhao, *ACS Catal.*, 2018, **8**, 1186–1191.
31 P. H. van Langevelde, I. Katsounaros and M. T. M. Koper, *Joule*, 2021, **5**, 290–294.
32 W. J. Sun, H. Q. Ji, L. X. Li, H. Y. Zhang, Z. K. Wang, J. H. He and J. M. Lu, *Angew. Chem., Int. Ed.*, 2021, **60**, 22933–22939.
33 H. Niu, Z. Zhang, X. Wang, X. Wan, C. Shao and Y. Guo, *Adv. Funct. Mater.*, 2021, **31**, 2008533.
34 N. C. Kani, J. A. Gauthier, A. Prajapati, J. Edgington, I. Bordawekar, W. Shields, M. Shields, L. C. Seitz, A. R. Singh and M. R. Singh, *Energy Environ. Sci.*, 2021, **14**, 6349–6359.
35 P. Gao, Z. H. Xue, S. N. Zhang, D. Xu, G. Y. Zhai, Q. Y. Li, J. S. Chen and X. H. Li, *Angew. Chem., Int. Ed.*, 2021, **60**, 20711–20716.
36 Q. Hu, Y. Qin, X. Wang, Z. Wang, X. Huang, H. Zheng, K. Gao, H. Yang, P. Zhang, M. Shao and C. He, *Energy Environ. Sci.*, 2021, **14**, 4989–4997.
37 M. Li, X. Liu, L. Wang, F. Hou, S. X. Dou and J. Liang, *EcoMat*, 2021, **3**, 1–26.
38 Y. Wang, A. Xu, Z. Wang, L. Huang, J. Li, F. Li, J. Wicks, M. Luo, D. H. Nam, C. S. Tan, Y. Ding, J. Wu, Y. Lum, C. T. Dinh, D. Sinton, G. Zheng and E. H. Sargent, *J. Am. Chem. Soc.*, 2020, **142**, 5702–5708.
39 G. F. Chen, Y. Yuan, H. Jiang, S. Y. Ren, L. X. Ding, L. Ma, T. Wu, J. Lu and H. Wang, *Nat. Energy*, 2020, **5**, 605–613.
40 S. B. Patil, T. R. Liu, H. L. Chou, Y. Bin Huang, C. C. Chang, Y. C. Chen, Y. S. Lin, H. Li, Y. C. Lee, Y. J. Chang, Y. H. Lai, C. Y. Wen and D. Y. Wang, *J. Phys. Chem. Lett.*, 2021, **12**, 8121–8128.
41 S. B. Patil, H. L. Chou, Y. M. Chen, S. H. Hsieh, C. H. Chen, C. C. Chang, S. R. Li, Y. C. Lee, Y. S. Lin, H. Li, Y. J. Chang, Y. H. Lai and D. Y. Wang, *J. Mater. Chem. A*, 2021, **9**, 1230–1239.
42 S. B. Patil and D. Y. Wang, *Small*, 2020, **16**, 1–44.
43 C. C. Chang, S. R. Li, H. L. Chou, Y. C. Lee, S. Patil, Y. S. Lin, C. C. Chang, Y. J. Chang and D. Y. Wang, *Small*, 2019, **15**, 1–7.
44 R. Jia, Y. Wang, C. Wang, Y. Ling, Y. Yu and B. Zhang, *ACS Catal.*, 2020, **10**, 3533–3540.
45 S. Xu, D. C. Ashley, H. Y. Kwon, G. R. Ware, C. H. Chen, Y. Losovyj, X. Gao, E. Jakubikova and J. M. Smith, *Chem. Sci.*, 2018, **9**, 4950–4958.
46 I. Taniguchi, N. Nakashima, K. Matsushita and K. Yasukouchi, *J. Electroanal. Chem. Interfacial Electrochem.*, 1987, **224**, 199–209.
47 S. Guo, K. Heck, S. Kasiraju, H. Qian, Z. Zhao, L. C. Grabow, J. T. Miller and M. S. Wong, *ACS Catal.*, 2018, **8**, 503–515.
48 J. Liu, T. Cheng, L. Jiang, A. Kong and Y. Shan, *ACS Appl. Mater. Interfaces*, 2020, **12**, 33186–33195.
49 Y. Wang, Y. Yu, R. Jia, C. Zhang and B. Zhang, *Natl. Sci. Rev.*, 2019, **6**, 730–738.
50 S. Garcia-Segura, M. Lanzarini-Lopes, K. Hristovski and P. Westerhoff, *Appl. Catal., B*, 2018, **236**, 546–568.
51 J. Gao, B. Jiang, C. Ni, Y. Qi, Y. Zhang, N. Oturan and M. A. Oturan, *Appl. Catal., B*, 2019, **254**, 391–402.
52 J. M. McEnaney, S. J. Blair, A. C. Nielander, J. A. Schwalbe, D. M. Koshy, M. Cargnello and T. F. Jaramillo, *ACS Sustainable Chem. Eng.*, 2020, **8**, 2672–2681.
53 A. Thornton, P. Pearce and S. A. Parsons, *J. Hazard. Mater.*, 2007, **147**, 883–889.
54 J. H. Jang, A. Gaur, H. J. Song and J. Park, *Chem. Pap.*, 2011, **65**, 437–446.
55 L. Su, D. Han, G. Zhu, H. Xu, W. Luo, L. Wang, W. Jiang, A. Dong and J. Yang, *Nano Lett.*, 2019, **19**, 5423–5430.
56 Z. Y. Wu, M. Karamad, X. Yong, Q. Huang, D. A. Cullen, P. Zhu, C. Xia, Q. Xiao, M. Shakouri, F. Y. Chen, J. Y. Kim, Y. Xia, K. Heck, Y. Hu, M. S. Wong, Q. Li, I. Gates, S. Siahrostami and H. Wang, *Nat. Commun.*, 2021, **12**, 1–10.

57 J. Li, G. Zhan, J. Yang, F. Quan, C. Mao, Y. Liu, B. Wang, F. Lei, L. Li, A. W. M. Chan, L. Xu, Y. Shi, Y. Du, W. Hao, P. K. Wong, J. Wang, S. X. Dou, L. Zhang and J. C. Yu, *J. Am. Chem. Soc.*, 2020, **142**, 7036–7046.

58 A. Wütscher, T. Eckhard, D. Hiltrop, K. Lotz, W. Schuhmann, C. Andronescu and M. Muhler, *ChemElectroChem*, 2019, **6**, 514–521.

59 Z. Chen, A. Jaworski, J. Chen, T. M. Budnyak, I. Szewczyk, A. Rokicińska, R. Dronskowski, N. Hedin, P. Kuśtrowski and A. Slabon, *Dalton Trans.*, 2021, **50**, 6857–6866.

60 S. Monti, G. Barcaro, W. A. Goddard and A. Fortunelli, *ACS Nano*, 2021, **15**, 6369–6385.

61 F. Calle-Vallejo, M. Huang, J. B. Henry, M. T. M. Koper and A. S. Bandarenka, *Phys. Chem. Chem. Phys.*, 2013, **15**, 3196–3202.

62 J. K. Nørskov, J. Rossmeisl, A. Logadottir, L. Lindqvist, J. R. Kitchin, T. Bligaard and H. Jónsson, *Appl. Catal., B*, 2004, **108**, 17886–17892.

63 Z. Ma, T. Thersleff, A. L. Görne, N. Cordes, Y. Liu, S. Jakobi, A. Rokicinska, Z. G. Schichtl, R. H. Coridan, P. Kustrowski, W. Schnick, R. Dronskowski and A. Slabon, *ACS Appl. Mater. Interfaces*, 2019, **11**, 19077–19086.

64 Z. Ma, A. Jaworski, J. George, A. Rokicinska, T. Thersleff, T. M. Budnyak, G. Hautier, A. J. Pell, R. Dronskowski, P. Kuśtrowski and A. Slabon, *J. Phys. Chem. C*, 2019, **124**, 152–160.

65 C. Zhu, S. Monti and A. P. Mathew, *ACS Nano*, 2018, **12**, 7028–7038.

66 Scientific Computing & Modelling NV, *ADF Manual Amsterdam Modeling Suite 2019*, 2019.

67 P. Giannozzi, S. Baroni, N. Bonini, M. Calandra, R. Car, C. Cavazzoni, D. Ceresoli, G. L. Chiarotti, M. Cococcioni, I. Dabo, A. Dal Corso, S. De Gironcoli, S. Fabris, G. Fratesi, R. Gebauer, U. Gerstmann, C. Gougoussis, A. Kokalj, M. Lazzeri, L. Martin-Samos, N. Marzari, F. Mauri, R. Mazzarello, S. Paolini, A. Pasquarello, L. Paulatto, C. Sbraccia, S. Scandolo, G. Sclauzero, A. P. Seitsonen, A. Smogunov, P. Umari and R. M. Wentzcovitch, *J. Phys.: Condens. Matter*, 2009, **21**, 395502.

68 J. P. Perdew, K. Burke and M. Ernzerhof, *Phys. Rev. Lett.*, 1996, **77**, 3865–3868.

69 G. Stefan, *J. Comput. Chem.*, 2006, **27**, 1787–1799.

70 K. S. W. Sing, D. H. Everett, R. A. W. Haul, L. Moscou, R. A. Pierotti, J. Rouquerol and T. Siemieniewska, *Pure Appl. Chem.*, 1985, **57**, 603–619.

71 P. P. Sharma, J. Wu, R. M. Yadav, M. Liu, C. J. Wright, C. S. Tiwary, B. I. Yakobson, J. Lou, P. M. Ajayan and X.-D. Zhou, *Angew. Chem.*, 2015, **127**, 13905–13909.

72 A. C. Ferrari, *Solid State Commun.*, 2007, **143**, 47–57.

73 I. Szewczyk, A. Rokicińska, M. Michalik, J. Chen, A. Jaworski, R. Aleksis, A. J. Pell, N. Hedin, A. Slabon and P. Kuśtrowski, *Chem. Mater.*, 2020, **32**, 7263–7273.

74 L. Zhang, L. Ding, G. Chen, X. Yang and H. Wang, *Angew. Chem.*, 2019, **131**, 2638–2642.

75 J. Lim, C. Y. Liu, J. Park, Y. H. Liu, T. P. Senftle, S. W. Lee and M. C. Hatzell, *ACS Catal.*, 2021, **11**, 7568–7577.